doi:10.1093/brain/awr250 Brain 2011: 134; 3369–3383 | 3369

BRAIN
A JOURNAL OF NEUROLOGY

X-linked Angelman-like syndrome caused by Slc9a6 knockout in mice exhibits evidence of endosomal–lysosomal dysfunction

Petter Strømme,[1,2,3] Kostantin Dobrenis,[1] Roy V. Sillitoe,[1] Maria Gulinello,[4] Nafeeza F. Ali,[1] Cristin Davidson,[1] Matthew C. Micsenyi,[1] Gloria Stephney,[1] Linda Ellevog,[3,5] Arne Klungland[3,5] and Steven U. Walkley[1]

1 Dominick P. Purpura Department of Neuroscience, Rose F. Kennedy Centre, Albert Einstein College of Medicine, Bronx, NY 10461, USA
2 Women and Children's Division, Department of Clinical Neurosciences for Children, Oslo University Hospital, Ullevål Hospital, 0424 Oslo, Norway
3 Faculty of Medicine, University of Oslo, 0316 Oslo, Norway
4 Behavioural Core Facility, Department of Neuroscience, Albert Einstein College of Medicine, Bronx, NY 10461, USA
5 Centre for Molecular Biology and Neuroscience and Institute of Medical Microbiology, Oslo University Hospital, Rikshospitalet, 0424 Oslo, Norway

Correspondence to: Steven U. Walkley,
Department of Neuroscience,
Rose F. Kennedy Centre,
Albert Einstein College of Medicine,
Bronx, NY 10461,
USA
E-mail: steve.walkley@einstein.yu.edu

Mutations in solute carrier family 9 isoform 6 on chromosome Xq26.3 encoding sodium–hydrogen exchanger 6, a protein mainly expressed in early and recycling endosomes are known to cause a complex and slowly progressive degenerative human neurological disease. Three resulting phenotypes have so far been reported: an X-linked Angelman syndrome-like condition, Christianson syndrome and corticobasal degeneration with tau deposition, with each characterized by severe intellectual disability, epilepsy, autistic behaviour and ataxia. Hypothesizing that a sodium–hydrogen exchanger 6 deficiency would most likely disrupt the endosomal–lysosomal system of neurons, we examined *Slc9a6* knockout mice with tissue staining and related techniques commonly used to study lysosomal storage disorders. As a result, we found that sodium–hydrogen exchanger 6 depletion leads to abnormal accumulation of GM2 ganglioside and unesterified cholesterol within late endosomes and lysosomes of neurons in selective brain regions, most notably the basolateral nuclei of the amygdala, the CA3 and CA4 regions and dentate gyrus of the hippocampus and some areas of cerebral cortex. In these select neuronal populations, histochemical staining for β-hexosaminidase activity, a lysosomal enzyme involved in the degradation of GM2 ganglioside, was undetectable. Neuroaxonal dystrophy similar to that observed in lysosomal disease was observed in the cerebellum and was accompanied by a marked and progressive loss of Purkinje cells, particularly in those lacking the expression of Zebrin II. On behavioural testing, *Slc9a6* knockout mice displayed a discrete clinical phenotype attributable to motor hyperactivity and cerebellar dysfunction. Importantly, these findings show that sodium–hydrogen exchanger 6 loss of function in the *Slc9a6*-targeted mouse model leads to compromise of endosomal–lysosomal function similar to lysosomal disease and to conspicuous neuronal abnormalities in specific brain regions, which in concert could provide a unified explanation for the cellular and clinical phenotypes in humans with *SLC9A6* mutations.

Received May 4, 2011. Revised July 13, 2011. Accepted July 30, 2011. Advance Access publication September 29, 2011

Keywords: amygdala; Angelman syndrome; endosome; ganglioside; lysosomal storage disorder

Abbreviations: LAMP2 = lysosomal-associated membrane protein 2; NHE = sodium–hydrogen exchanger; *SLC9A6* = solute carrier family 9 isoform 6; X-GAL = 5-bromo-4-chloro-3-indolyl-β-D-galactopyranoside; X-HEX = 5-bromo-4-chloro-3-indolyl-*N*-acetyl-β-D-glucosaminide

Introduction

The sodium–hydrogen exchanger (NHE) proteins belong to a large family of transporters encoded by members of the solute carrier (SLC) gene superfamily (He *et al.*, 2009). Defects of one of these transporters, sodium–hydrogen exchanger 6 (NHE6), encoded by *SLC9A6* at the locus Xq26.3 was first detected in males with intellectual disability, microcephaly, epilepsy, ataxia and behavioural abnormalities mimicking Angelman syndrome (Gilfillan *et al.*, 2008). Following the identification of other patients with *SLC9A6* mutations, three clinical phenotypes have emerged: first, the most common clinical manifestation to date appears to be an X-linked Angelman syndrome-like condition; a second Angelman syndrome-like phenotype, also known as Christianson syndrome (OMIM #300243) (Christianson *et al.*, 1999), which appears to show a divergent phenotype in older patients (Gilfillan *et al.*, 2008; Schroer *et al.*, 2010); finally, a third phenotype presents with corticobasal degeneration and tau deposition and with severe intellectual disability and autistic behaviour (Garbern *et al.*, 2010). Since *SLC9A6* loss of function is an established cause of neurodegenerative disease, our goal was to explore the cellular mechanisms behind the degenerative process.

The NHE proteins are known to play an important role in the fine-tuning of organellar pH. Normally, a decrease of pH occurs from cytosol (pH 7.2) to the early endosome (pH 6.3) and to the lysosome (pH 4.7) [see Casey *et al*. (2010)]. As an evolutionarily conserved mechanism for protection against excess acidification, cation–H^+ exchangers couple the transfer of H^+ across biological membranes to the counter transport of monovalent cations such as Na^+ or K^+. In order to carry out this task, mammals are known to possess nine NHE isoforms, NHE1–9 (encoded by *SLC9A1–9*); for a review see Oghaki *et al*. (2011). NHE1–NHE5 are believed to be localized to the plasma membrane and NHE7 and NHE8 to the Golgi and trans-Golgi network. NHE6 localizes to early and recycling endosomes and transiently associates with the cell surface, whereas NHE9 localizes mostly to late recycling endosomes (Nakamura *et al.*, 2005). Three important functions of the NHE6 protein have been suggested: pH regulation through its function as a transporter of Na^+ in and H^+ out of the endosomal compartment; endosomal volume regulation; and regulation of the rate of surface receptor recycling (Brett *et al.*, 2002).

Given the putative role of NHE6 in early endosomal function, we hypothesized that its absence might cause disturbances of endosomal–lysosomal function, possibly leading to storage of materials within neurons. We therefore examined *Slc9a6* knockout mice with a panel of methods used to assess the consequences of lysosomal dysfunction, including secondary accumulation of glycolipids in the brain (Walkley, 1998; Walkley and Vanier, 2009). Here, we demonstrate that NHE6 depletion in mice leads to abnormal accumulation of GM2 ganglioside and unesterified cholesterol within late endosomes and lysosomes in neurons within selective brain regions, most notably the amygdala and CA3 and CA4 regions of the hippocampus, and to extensive degeneration of cerebellar Purkinje cells. The cellular changes in neurons were similar to those observed in various lysosomal disorders and may explain both the pathological and clinical disease features in humans with mutations in *SLC9A6*.

Materials and methods

Animals, messenger RNA assay and tissue collection

All procedures were carried out in accordance with The Institutional Animal Care and Use Committee of the Albert Einstein College of Medicine. The *Slc9a6* knockout mice (Stock# 005843, strain name B6.129P2-Slc9a6<tm1Dgen) were obtained from Jackson Laboratories (see also JAX Mice Database). The model was engineered by inserting the *LacZ* reporter gene, which encodes β-galactosidase into the *Slc9a6* genomic locus (Deltagen). Hemizygous $Slc9a6^{-/X}$ females were bred with wild-type $Slc9a6^{+/Y}$ or hemizygous $Slc9a6^{-/Y}$ males resulting overall in the production of wild-type $Slc9a6^{+/+}$, hemizygous $Slc9a6^{-/X}$ and homozygous $Slc9a6^{-/-}$ females, and hemizygous $Slc9a6^{-/Y}$ and wild-type $Slc9a6^{+/Y}$ males (Supplementary Fig. 1A). As the inserted *LacZ*-Neo cassette created a larger polymerase chain reaction product, the genotyping was based upon expected band sizes (Supplementary Fig. 1B) and inspection of external genitalia at 2 weeks of gestation. In all experiments, male $Slc9a6^{-/Y}$ and female $Slc9a6^{-/-}$ mice were used as mutants and wild-type $Slc9a6^{+/Y}$ males as controls. On average, four mice of each genotype were used in each experiment.

The *LacZ*-Neo cassette inserted into exon 6 of *Slc9a6* introduces a stop codon and a polyadenylation termination signal. The expected consequence of this manipulation would be termination of, or severely reduced transcription behind, the *LacZ*-Neo cassette. We therefore assayed the expression of various exons affected by the *LacZ*-Neo cassette by quantitative real-time polymerase chain reaction on total messenger RNA from wild-type and *Slc9a6* mutant mice (Fig. 1A). These methods are further detailed in the Supplementary material. The primers are listed in Supplementary Table 1.

Mice used for tissue collection were deeply anaesthetized with sodium pentobarbital (150 mg/kg) and perfused transcardially with 0.9% saline followed by excision of the right cerebral hemisphere, which was immediately frozen for biochemical analysis. Transcardial fixation perfusion was then performed using 4% paraformaldehyde in 0.1 M phosphate buffer. The remaining cerebral and cerebellar tissues were excised and immersion fixed overnight before being transferred to 0.1 M phosphate buffer for storage at 4°C.

Staining procedures

Antibodies and reagents used for staining procedures are included in the Supplementary material.

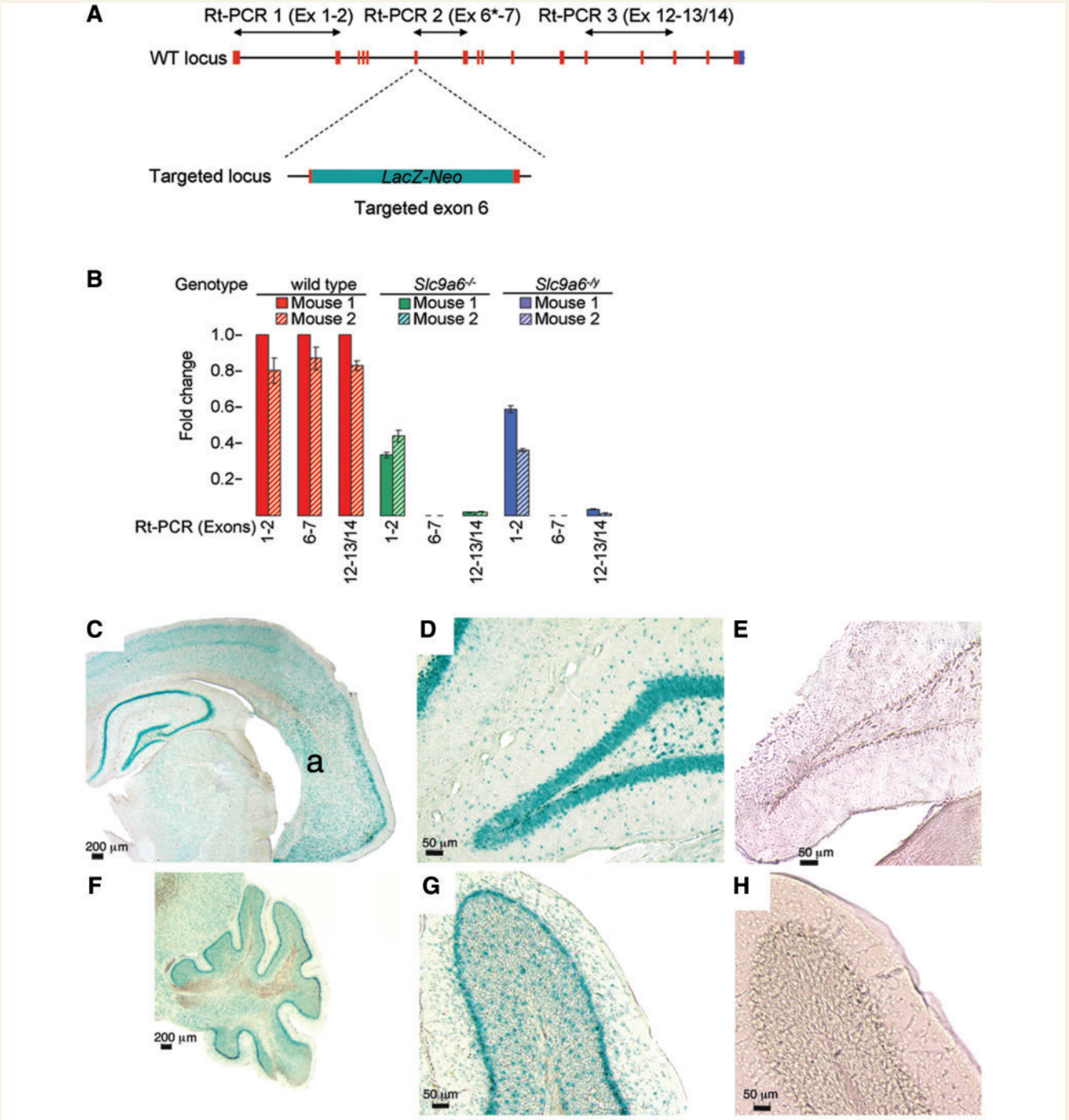

Figure 1 *Slc9a6* expression in the mouse brain. (**A**) Schematic drawing illustrating the insertion of the *LacZ*-Neo cassette into exon 6 and the positioning of the primers used in quantitative real-time polymerase chain reaction (Rt-PCR) to assay messenger RNA levels. Asterisk = forward primer in exon 6 is within the deleted 847–898 region. (**B**) Real-time polymerase chain reaction on total RNA from cerebral cortex demonstrated abundant messenger RNA obtained with all three primer sets in wild-type control mice (red bars). In the female (green bars) and male (blue bars) mutants, a moderate but significant reduction of transcription initiation is indicated by real-time polymerase chain reaction with primer set 1, whereas messenger RNA from targeted exon 6 (primer set 2) is absent. Messenger RNA containing exons 12–14 (primer set 3) is virtually absent in mutant mice. (**C–H**) Results of X-GAL staining revealing *LacZ* gene product expression driven by the endogenous *Slc9a6* promoter. (**C**) Coronal section of the brain of *Slc9a6*$^{-/Y}$ mouse at a level that includes the hippocampus and the dorsolateral amygdala nucleus (a). Positive blue–green X-GAL staining reveals widespread expression in the brain, particularly in neurons of the hippocampus. (**D**) Positive staining in the dentate gyrus of the hippocampus. (**E**) Dentate gyrus of the hippocampus from wild-type used as a negative control shows absence of background staining after X-GAL incubation. (**F** and **G**) Markedly positive X-GAL staining in the Purkinje cell layer of the cerebellum in a *Slc9a6*$^{-/Y}$ mouse. (**H**) Similar to **E**, wild-type cerebellum shows absence of X-GAL reactivity.

Tissue sections were cut on a Leica VT-1000S vibratome. Free-floating sections were used for immunohistochemistry as described previously (McGlynn *et al.*, 2004; Sillitoe *et al.*, 2008). Briefly, for immunoperoxidase labelling, sections were blocked for 1 h in 1% bovine serum albumin, 1.5% normal goat serum and 0.02% saponin in phosphate-buffered saline. Tissue was next incubated with primary antibodies in diluent (1% bovine serum albumin, 1% normal goat serum, and 0.02% saponin in phosphate-buffered saline) overnight at 4°C. After washing, biotinylated secondary antibodies were applied, followed by washing and incubation with VECTASTAIN® avidin and biotinylated horseradish peroxidase macromolecular complex (ABC) kit (Vector Laboratories). Sections were then stained with 3,3-diaminobenzidine substrate kit for peroxidase (Vector Laboratories) and further counterstained with Nissl before mounting with Permount (Fisher). Immunofluorescence labelling included blocking for 1.5 h with 1% bovine serum albumin, 10% normal goat serum and 0.02% saponin in phosphate-buffered saline, followed by primary antibody application with 1% bovine serum albumin, 5% normal goat serum and 0.02% saponin in phosphate-buffered saline overnight at 4°C. Incubation with fluorescent secondary antibodies was followed by tissue mounting using Prolong Antifade reagent (Invitrogen). Filipin labelling of unesterified cholesterol was performed by incubating pre-washed tissue sections in the working solution for 20 min. 5-Bromo-4-chloro-3-indolyl-β-D-galactopyranoside (X-GAL) was used to detect *LacZ* transgene expression. A 40 mg/ml X-GAL stock solution was diluted to 1 mg/ml working concentration in reaction buffer (5 mM potassium ferricyanide, 5 mM potassium ferrocyanide and 2 mM magnesium chloride in 10 mM phosphate-buffered saline, pH 7.2, at room temperature). Tissue sections were cut at 40 μm and washed in cold phosphate-buffered saline, followed by washes with reaction buffer. Sections were then incubated in reaction mixture containing X-GAL at 37°C for 3 h, followed by washes with cold phosphate-buffered saline. Mounting was done directly onto gel-coated slides using 10% phosphate-buffered saline/90% glycerol. For the analysis of cerebellar compartmentalization serial, 40-μm thick coronal sections were cut on a cryostat (Leica CM3050) and collected as free-floating sections in phosphate-buffered saline. Immunohistochemistry was carried out similar to that previously described. Briefly, tissue sections were washed thoroughly, blocked with 1.5% normal goat serum for 1 h at room temperature and then incubated in 0.1 M phosphate-buffered saline buffer containing 0.1% Triton-X and primary antibodies for 16–18 h at room temperature. Tissue sections were then washed three times in phosphate-buffered saline and incubated in secondary antibodies for 2 h at room temperature. After three final rinses in phosphate-buffered saline, the tissue sections were mounted on electrostatically coated slides and coverslipped using Fluoro-Gel (Electron Microscopy Sciences).

Saline perfused, rapidly frozen cerebral hemispheres from *Slc9a6*$^{-/Y}$ versus *Slc9a6*$^{+/Y}$ mice were also analysed biochemically to quantitatively analyse the expression of GM2, GM3 and related gangliosides using methods identical to those published recently (Micsenyi *et al.*, 2009; Zhou *et al.*, 2011). Additionally, western blots were performed to analyse for the presence of hyperphosphorylated tau. The methodology for the western blot procedures is provided in the Supplementary material.

For histochemical detection of lysosomal β-hexosaminidase (E.C. 3.2.1.52), freshly cut 40 μm thick vibratome sections from 4% paraformaldehyde-fixed tissue were assayed with 5-bromo-4-chloro-3-indolyl-*N*-acetyl-β-D-glucosaminide (X-HEX) (Research Organics #1175B). Free-floating sections were incubated for 19 h at 37°C with 2.5 mg/ml X-HEX (from a 40 mg/ml stock in dimethylsulphoxide) in 0.1 M citric acid/0.2 M sodium phosphate buffer, pH 4.5, containing 0.5 mM potassium ferrocyanide and 0.5 mM potassium ferricyanide. The reaction was terminated on ice by washing first with cold 0.1 M citric acid/0.2 M sodium phosphate buffer alone, followed by five washes in 0.15 M phosphate-buffered saline, pH 7.4. Sections were mounted with 10% phosphate-buffered saline/90% glycerol and sealed with nail hardener.

Tissue imaging and nomenclature

Widefield microscopy was carried out using either a Leica DM5500 microscope running Leica LAS-AF software (Leica DFC360 FX) for cerebellar patterned Purkinje cell loss studies or an Olympus AX70 upright epifluorescence microscope equipped with a MagnaFire CCD camera (Optronics) for all other studies. Confocal fluorescence imaging was performed using a Zeiss Meta Duo V2 laser scanning confocal microscope. Immunofluorescence images were acquired with a ×63 (1.4 numerical aperture) oil objective. All raw data were imported into Adobe Photoshop CS4 and adjusted for brightness and contrast, and occasionally for colour. The nomenclature and labelling of subnuclei of the amygdala complex were adopted from Paxinos and Watson (1986). The cerebellar lobules were indicated by Roman numerals according to Larsell (1952), cerebellar stripe nomenclature was according to Sillitoe and Hawkes (2002) and the cerebellar transverse zones were labelled according to Ozol *et al*. (1999).

Electron microscopy

Brain tissue for electron microscopy was prepared as previously described (Micsenyi *et al.*, 2009). Following fixation of tissue described above, blocks for electron microscopy were post-fixed in 2.5% glutaraldehyde in 0.1 M cacodylate buffer then rinsed in 0.1 M cacodylate buffer. Samples were next incubated in 1% osmium tetroxide in 0.1 M cacodylate buffer, followed by dehydration in graded alcohols and acetonitrile. Blocks were infiltrated overnight in 1:1 EPON^{TM}/acetonitrile, followed by infiltration and embedding with whole EPON^{TM}. Sections were then cut with an ultramicrotome and stained with uranyl acetate and lead citrate. In some cases, vibratome sections were treated with antibodies to GM2 ganglioside and processed for peroxidase labelling, followed by EPON^{TM} embedding and sectioning as described. Electron microscopy was performed using a Philips CM10 electron microscope.

Behavioural studies

Only male *Slc9a6*$^{-/Y}$ ($n = 6$) and male wild-type *Slc9a6*$^{+/Y}$ ($n = 10$) mice were used for behavioural assays. Open field activity was assessed using Viewer Software (Bobserve) in a 39 × 39 cm arena for 6 min with the middle of the body of the animal defined as the criteria point for tracking and zone entry. Locomotor activity was assessed as the total track length and exploration by the number of rears (scored manually). Anxiety-like behaviour (thigmotaxis) was assessed by central zone exploration (number of entries, centre track length and duration of time spent in the centre) (Choleris *et al.*, 2001). The central zone was defined as a 15 × 15 cm area in the centre of the box. Motor coordination was assessed in the balance beam assay as the latency to cross a round beam (1.5 cm diameter) and number of slips made while crossing (Stanley *et al.*, 2005). To minimize variation and acclimatize mice to the task, mice were first pre-trained to walking over a flat wooden plank (6 cm wide) with a brightly lit start area and a goal box with a hide containing a palatable food (cocoa crispy) until they reliably and readily crossed the plank (two or three trials).

Mice were pre-exposed to the food for 2–4 days prior to reduce neophobia. Methods used for testing spatial memory in the object placement task (Ennaceur and Meliani, 1992) are detailed in the Supplementary material. Behavioural assays were analysed with one-way ANOVA tests. *P*-values 0.05 were considered to be statistically significant.

Web resources

Alan Institute for Brain Science: http://mouse.brain-map.org/welcome.do
Deltagen: http://www.informatics.jax.org/external/ko/deltagen/1688_MolBio.html
Jackson laboratories: http://jaxmice.jax.org/protocolsdb/
JAX Mice Database B6.129P2-*Slc9a6*^{tm1Dgen}/J: http://jaxmice.jax.org/strain/005843.html
Online Mendelian Inheritance in Man (OMIM): http://www.ncbi.nlm.nih.gov/Omim

Results

Tissue *Slc9a6* expression

Quantitative real-time polymerase chain reaction at the *Slc9a6* targeted loci demonstrated successful transcription termination in cerebral cortex (Fig. 1A and B) in *Slc9a6*$^{-/Y}$ and *Slc9a6*$^{-/-}$ mice as a result of the tm1 termination region inserted after the *LacZ*-Neo gene. Abundant full-length Slc9a6 messenger RNA was detected in cerebral cortex from wild-type mice. Intense positive X-GAL staining, indicating the presence of targeted *Slc9a6*, was observed not only in the molecular layer of the cerebellum and hippocampus, but also in the cortical and subcortical regions, including the amygdala (Fig. 1C–H). This correlated with the genome-wide atlas of gene expression in the adult mouse brain (Lein *et al.*, 2007); see also http://mouse.brain-map.org/welcome.do.

Cellular pathology

Histopathological examination of brain for evidence of disturbances of lysosomal function revealed regional accumulation of GM2 ganglioside in mutant mice (Fig. 2). The staining in wild-type littermate age-matched controls showed absent to rarely occurring positive granules (Fig. 2C, F and G) as previously reported (Goodman and Walkley, 1996). GM2 ganglioside accumulation was particularly prominent in the basolateral nuclei of the amygdala complex. Especially in *Slc9a6*$^{-/-}$ (female) mice, affected neurons in mice as young as 8 weeks exhibited large amounts of densely stained material (Fig. 2A and B). GM2 ganglioside was also present in several of these same nuclei of the amygdala of *Slc9a6*$^{-/Y}$ (male) mice, but the staining here was less intense (data not shown). By 12 weeks of age, GM2 ganglioside-accumulating neurons were also observed in the CA3 and CA4 regions and the inner dentate gyrus of the hippocampus (Fig. 2D and E), as well as hypothalamus, fasciola cinereum and piriform cortex. The number and intensity of GM2 ganglioside-labelled cells observed was typically greater in older *Slc9a6* mutant mice compared with younger mutants. We also stained brain tissues for GM1, GM3 and GD3 gangliosides, and analysed brains biochemically for ganglioside expression levels, but found no differences between *Slc9a6* mutant mice and wild-type.

We examined tissues for activity of the lysosomal enzyme responsible for GM2 degradation (β-hexosaminidase) using an X-HEX histochemical reaction, in which this substrate when cleaved, forms an insoluble blue–green product at the site of enzyme activity. Remarkably, we found little to no evidence of active enzyme in neurons storing GM2 ganglioside (Fig. 3B and D), whereas comparable wild-type neurons showed robust staining (Fig. 3A and C). To determine whether the accumulated GM2 ganglioside was interfering with the histochemical stain, we also stained these same brain areas in mice with Niemann–Pick disease type C, which have normal β-hexosaminidase activity and also significant intraneuronal GM2 ganglioside accumulation (Walkley and Suzuki, 2004) and found levels of X-HEX staining comparable with wild-type (data not shown). We also performed X-HEX staining in mice with Sandhoff disease (OMIM #268800) caused by total β-hexosaminidase deficiency and as expected found no X-HEX staining (data not shown). Comparison of the degree of staining for LAMP2 and cathepsin D (data not shown) specifically in the CA3 and CA4 regions and the dentate gyrus of the hippocampus also revealed detectably greater staining in the *Slc9a6* mutant mice than in wild-type, consistent with an enhancement of the number of lysosomes in these neurons (Fig. 3E and F).

Filipin labelling in *Slc9a6*$^{-/-}$ mice demonstrated detectable amounts of unesterified cholesterol in cells of the basolateral amygdala in a manner similar to that observed for GM2 ganglioside (Fig. 4). As expected, and consistent with the earlier published data (Walkley and Vanier, 2009), neurons of wild-type mice showed no evidence of positive labelling with filipin (data not shown). Confocal microscopy of sections double labelled for GM2 ganglioside and unesterified cholesterol showed that in the amygdala, cholesterol and GM2 ganglioside, sequestration occurred in the same neurons but that the two substrates were largely segregated to different subcellular vesicular populations (Fig. 4A–C). Importantly, when GM2 ganglioside staining was combined with LAMP2 in immunofluorescence studies and analysed by confocal microscopy, the vast majority of the two markers was co-localized (Fig. 4D–F), indicating that the ganglioside accumulation occurred specifically in late endosomes and lysosomes. Cholesterol was also principally localized to LAMP2-positive vesicles (data not shown).

Considering the report by Garbern *et al.* (2010) that human *SLC9A6* mutations were characterized by tau deposition in brain, western blots were performed to determine whether changes could be detected in phosphorylated tau in brains of *Slc9a6* mutants. As shown in Supplementary Fig. 2, small elevations in hyperphosphorylated tau were found in soluble brain fractions in both hemizygous male and homozygous female *Slc9a6* mutant mice compared with age-matched wild-type.

Electron microscopy studies were also carried out on cerebral cortex, amygdala and cerebellum and several abnormalities and unusual features were observed in *Slc9a6* mutant mice. The cytoplasm of some neurons in the amygdala exhibited singular, non-membrane-bound structures resembling aggresomes (Fig. 5A and B), or one or more membrane-bound lysosomal-like inclusions

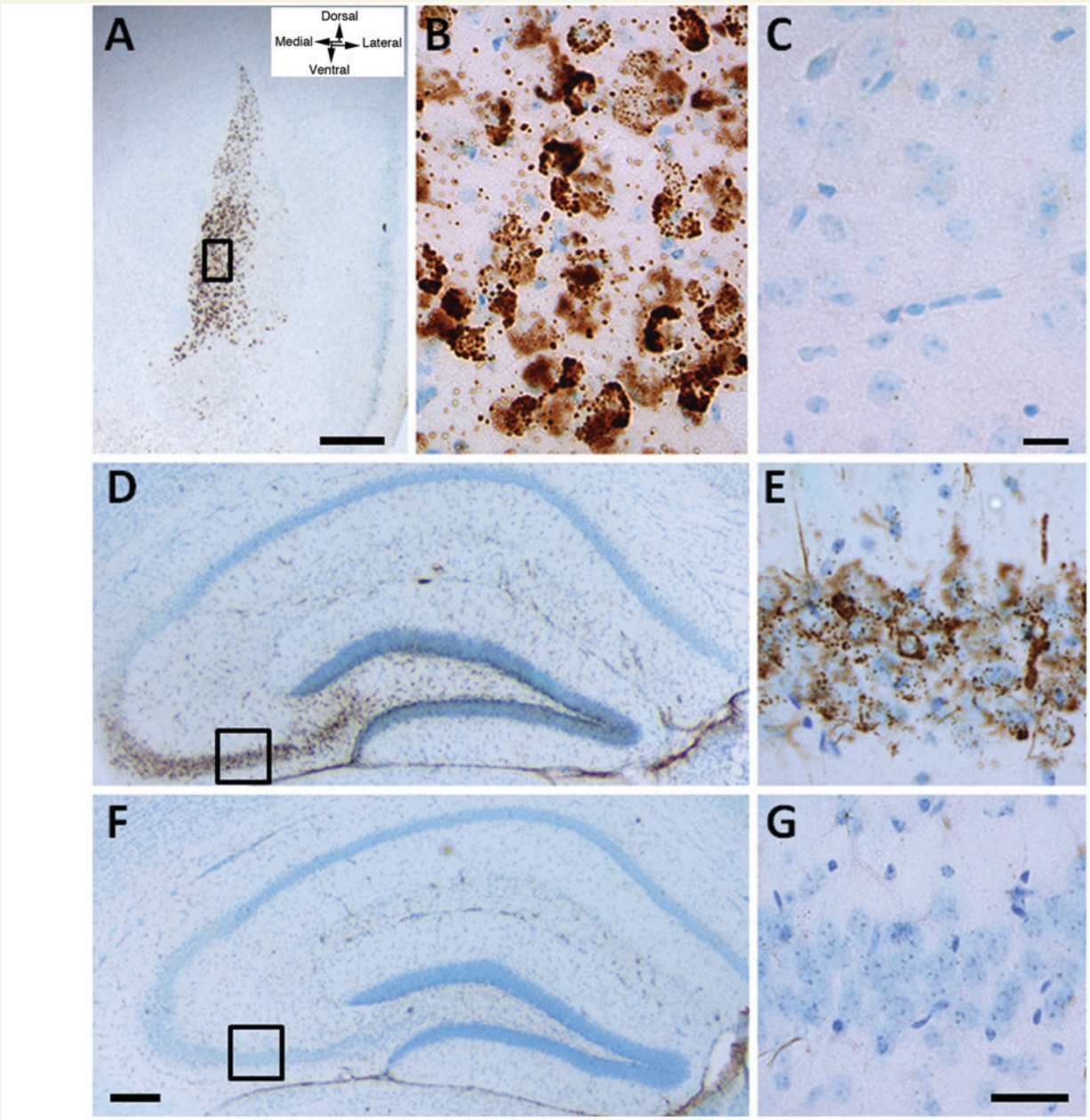

Figure 2 Immunostaining for GM2 ganglioside in 3-week and 8-week old *Slc9a6*$^{-/-}$ (female) mice. (**A**) At 3 weeks of age, prominent accumulation of GM2 ganglioside was observed in the anterior part of the basolateral amygdala. (**B**) At higher magnification, dense vesicular labelling occurred in individual neuronal cell bodies. (**C**) Immunoreactivity in the amygdala in an age-matched wild-type mouse from the same litter is near absent. (**D** and **E**) Accumulation of GM2 ganglioside was also seen in neurons of the CA3 and CA4 regions of the hippocampus of a *Slc9a6*$^{-/-}$ mouse at 8 weeks of age, as well as in the cell bodies of neurons in the dentate gyrus. (**F** and **G**) No GM2 immunoreactivity was found in these same regions of the hippocampus in an aged-matched wild-type mouse. Scale bars: **A** = 500 μm; **B** and **C** = 25 μm; **D** and **F** = 200 μm; **E** and **G** = 40 μm.

composed of a dense matrix (Fig. 5C and D). Some neurons in the amygdala and cerebral cortex, both with and without the inclusions indicated above, also exhibited an abnormal distribution of vesicular organelles with these appearing corralled near the Golgi and trans-Golgi network with other perikaryal regions appearing organelle deficient (Fig. 5E and F). Notably, neurons of the amygdala in mice exhibiting robust GM2 ganglioside storage typically contained multiple, large (0.5–1.0 μm diameter) loose-lamellar vesicles resembling storage bodies observed in some lysosomal diseases (Fig. 5G and H). The use of peroxidase-based immunoelectron microscopy confirmed that these vesicles were the sites of GM2 ganglioside storage (Fig. 5H, inset). In addition to these changes, nuclei of neurons in the amygdala and elsewhere were often lobulated excessively and/or their nucleoli were multiple in number and conspicuous by their electron density. In contrast to these findings in cerebral cortex and subcortical regions, electron

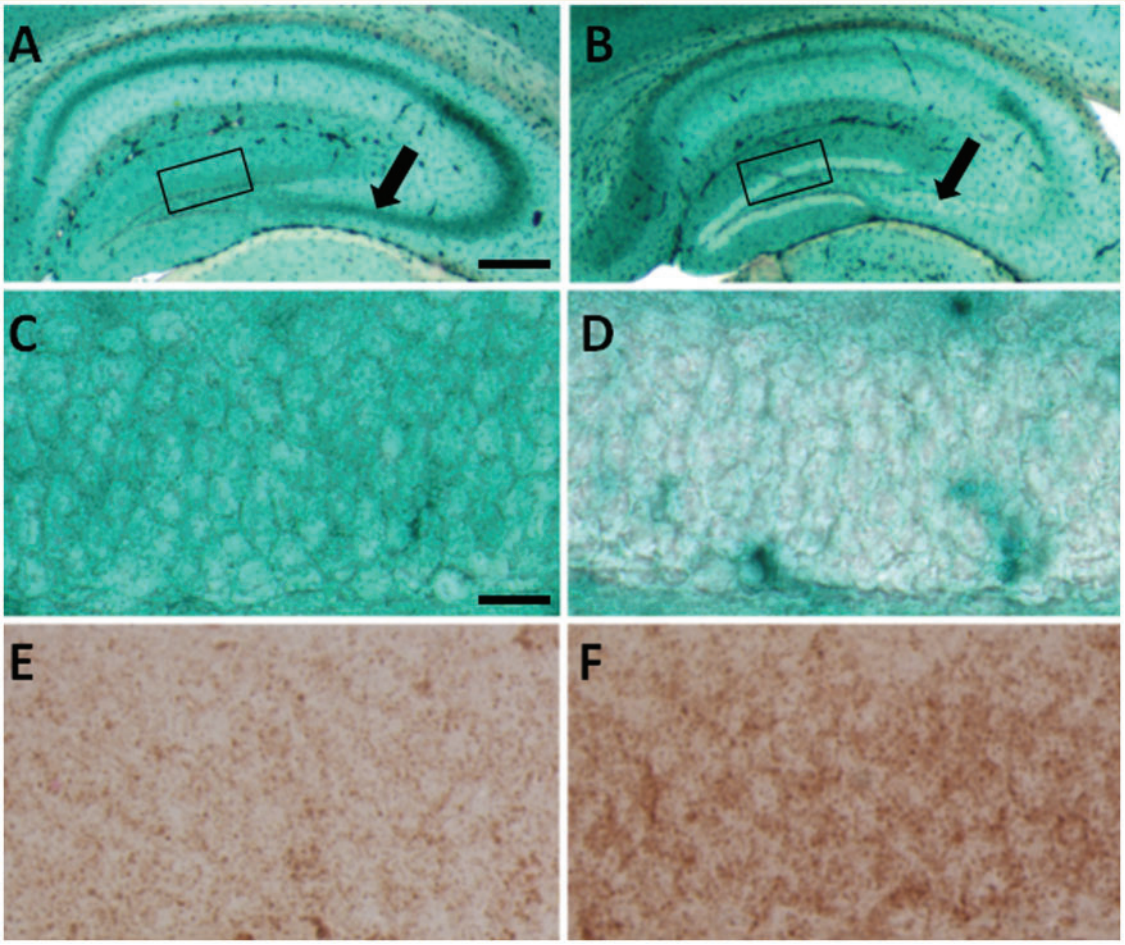

Figure 3 Histochemical staining to reveal β-hexosaminidase activity. (**A** and **C**) X-HEX staining in brain tissue from wild-type is robust as evidenced by blue/green labelling. (**B** and **D**) *Slc9a6*$^{-/-}$ mice show absent or greatly diminished X-HEX staining in the dentate gyrus (compare boxes in **A** and **B** which are enlarged as **C** and **D**, respectively) and in the CA3 and CA4 regions of the hippocampus (arrows in **A** and **B**). (**F** and **E**) LAMP2 (as well as cathepsin D, data not shown) staining performed to assess the extent of lysosomal involvement showed more intense labelling in the *Slc9a6*$^{-/-}$ mutant hippocampus (**F**) than in the wild-type (**E**). **E** and **F** represent areas of the dentate gyrus equivalent to those shown in **C** and **D**. Scale bars: **A** and **B** = 400 μm; **C–F** = 20 μm.

microscopy studies of cerebellar Purkinje cells did not reveal similar evidence of a lysosomal storage process.

Purkinje cell loss

The extensive and progressive loss of Purkinje cells observed in the cerebellum of *Slc9a6* mutant mice is illustrated in Fig. 6. Another striking feature was the presence of Purkinje cell axonal spheroids (Fig. 6C and E). The spheroids appeared similar to those observed in a number of lysosomal disorders, including Niemann–Pick disease type C (Walkley *et al.*, 2010). The loss of Purkinje cells was not random but instead occurred in a regular pattern of parasagittal stripes in the cerebellar vermis (Figs 7, 8A and B) and hemispheres (Fig. 8C). Patterned Purkinje cell loss was reminiscent of the compartmentalized expression of proteins such as Zebrin II/Aldolase C (Ahn *et al.*, 1994; Sillitoe and Hawkes, 2002). It is well known that Purkinje cells express many genes in a complex array of stripes that are unique to subsets of lobules (Sillitoe and Joyner, 2007). For example, Zebrin II is expressed in an array of stripes in lobules I–V and VIII, whereas the small heat shock protein 25 (HSP25) is expressed in stripes selectively in lobules VI/VII and IX/X. In contrast, Calbindin is expressed in all Purkinje cells and can be used to determine the extent of Purkinje cell degeneration in the cerebellum. We found in *Slc9a6*$^{-/Y}$ mice that loss of calbindin-expressing Purkinje cells occurred first within Zebrin II-negative stripes, whereas Purkinje cells in the Zebrin II-positive stripes were more resistant to the degenerative process (Fig. 7A–F). Purkinje cells in lobules VI/VII and IX/X, which express Zebrin II uniformly, were most resistant to neuronal degeneration (Fig. 8C). Interestingly, the general pattern of Purkinje cell stripe degeneration in *Slc9a6*$^{-/Y}$ mice was similar to the pattern of degeneration previously reported in Niemann–Pick disease type C mice (Sarna *et al.*, 2003). No obvious cell loss was detected in the cerebrum by light microscopy. This applied also to the amygdala and other areas in the cerebrum affected by GM2 ganglioside accumulation.

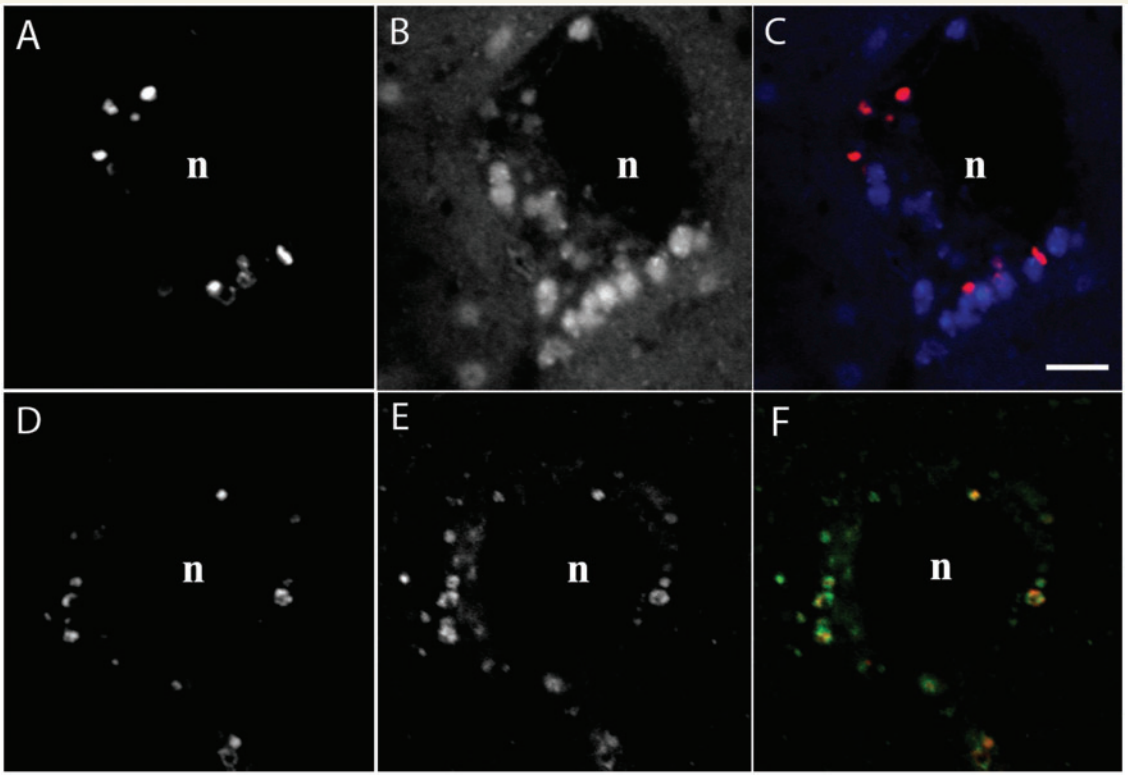

Figure 4 Confocal microscopy of GM2 ganglioside and cholesterol staining in neurons of the basolateral amygdala in a 3-week old *Slc9a6*$^{-/-}$ (female) mouse. (**A–C**) Combined GM2 ganglioside immunofluorescence and filipin labelling for cholesterol reveal that both substrates are sequestered in the same neurons but are largely not co-localized to the same vesicles. (**D–F**) Combined GM2 ganglioside and LAMP2 immunofluorescence demonstrate that the GM2 ganglioside accumulation is typically localized to LAMP2-positive late endosomes and lysosomes. Scale bars = 5 μm; n = nucleus.

Behaviour

In the open field, *Slc9a6*$^{-/Y}$ mice demonstrated a longer total track length (Fig. 9A) and a higher number of rears (Fig. 9B), both interpreted as a sign of modest but significant motor hyperactivity. There were no indications of differences in anxiety-like behaviour in the open field, as assessed by thigmotaxis (Supplementary Table 2). Motor coordination deficits were evident in the balance beam test as the mutants had a higher number of slips (Fig. 9C) and longer latency time to cross the beam (Fig. 9D). Gross ataxia, however, was not evident in *Slc9a6*$^{-/Y}$ mice in spite of the loss of many Purkinje cells, possibly reflective of other parts of the motor system being intact. In the object placement test of spatial memory, both mutants and wild-type mice could perform the task equivalently with a 20-min retention interval.

Genotype–phenotype correlation

In most cases, the *Slc9a6* mutant mice were not associated with an obvious clinical phenotype on simple clinical inspection, although mild motor hyperactivity and deficits in motor coordination were evident in older mice when specific behavioural tests were applied to *Slc9a6*$^{-/Y}$ males (Fig. 9). In some *Slc9a6*$^{-/-}$ mice, but not all, we observed premature death ~3 weeks of age. The *Slc9a6*$^{-/-}$ genotype seemed to coincide with more pronounced GM2 ganglioside accumulation in affected neurons. This increased sensitivity to *Slc9a6* loss of function in the female mouse brain could be due to stochastic events in our study and not necessarily genetic predetermination. Occasionally in X-linked disorders, an exaggerated phenotype is known to segregate with homozygous females, as has been reported in Retinoschisis (OMIM #312700) (Ali *et al.*, 2003). In human disease, the female homozygous state occurs rarely as it requires intermarriage. Unprovoked clinical seizures were not observed in *Slc9a6*$^{-/-}$ or *Slc9a6*$^{-/Y}$ mice.

Discussion

Our data indicate that *Slc9a6* loss of function leads to altered endosomal–lysosomal function in many neurons as evidenced by the accumulation of GM2 ganglioside and cholesterol. The loss of Purkinje neurons, while not linked here to any evident changes in endosomes or lysosomes within Purkinje cell somata, is nonetheless remarkably similar to the degenerative events that characterize cerebellar pathology in many lysosomal diseases. In human, *SLC9A6* mutation symptoms are usually not obvious at birth, but may present within the first year as developmental delay, seizures, ataxia, motor hyperactivity and stereotypies, and sometimes easily

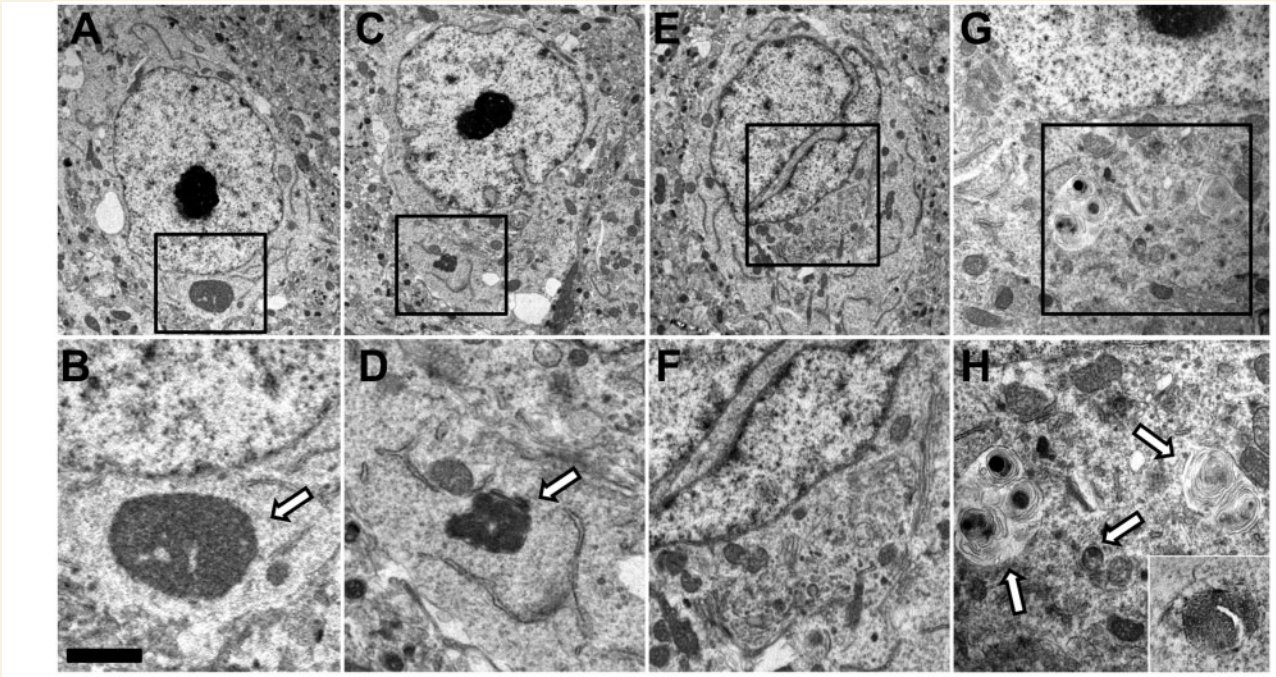

Figure 5 Electron microscopy studies of neurons in the amygdala of a 19-day-old *Slc9A6*$^{-/-}$ (female) mouse. (**A**) Neuron exhibiting a large non-membrane bound body resembling an aggresome (higher magnification shown in **B**). (**C**) Neuron exhibiting conspicuous double nucleolus and dispersed cytoplasm as well as a membrane-bound inclusion containing a dense storage matrix (higher magnification shown in **D**). (**E**) Neuron exhibiting a heavily lobulated nucleus and a collection of vesicular and other structures corralled near the Golgi and trans-Golgi network (higher magnification shown in **F**). (**G**) Neuron exhibiting conspicuous loose lamellar inclusions that by immunoelectron microscopy (higher magnification in **H**) were shown to exhibit GM2 ganglioside positivity. Scale bar = 1.9 μm (**A**), 0.5 μm (**B**), 4.0 μm (**C**), 1.0 μm (**D**), 3.15 μm (**E**), 1.4 μm (**F**), 1.6 μm (**G**), 1.0 μm (**H**) and 1.0 μm (inset, **H**).

provoked laughter (Gilfillan *et al.*, 2008), features also typical of Angelman syndrome (Williams *et al.*, 2006).

Solute carrier transporters are believed to play essential roles in cellular uptake and efflux of nutrients, neurotransmitters, metabolites and electrolytes (He *et al.*, 2009). Several of these transporters have been associated with inherited metabolic disease (Bergeron *et al.*, 2008). In mouse, intricate solute carrier expression patterns associated with neuroanatomical organization have been observed (Dahlin *et al.*, 2009). In the present study, we have documented widespread tissue expression of NHE6 throughout the cerebrum and cerebellum (Fig. 1C–H). The extent of NHE6 expression did not, however, coincide with those areas that seemed most vulnerable to develop tissue pathology such as the amygdala and CA3 and CA4 regions of the hippocampus. In the basolateral nuclei of the amygdala, NHE6 expression was not especially conspicuous, yet this was the site of massive GM2 ganglioside accumulation. Strong NHE6 tissue expression in the Purkinje cell layer of the cerebellum (Fig. 1F and G) coincided with Purkinje cell loss (Fig. 6), but without abnormal GM2 ganglioside accumulation or related evidence of endosomal or lysosomal dysfunction.

Evidence of endosomal–lysosomal dysfunction

Storage involving late endosomes and lysosomes of neurons and glia are a hallmark of most lysosomal diseases (Walkley, 1998, 2004*a*). In the present study, the accumulation of GM2 ganglioside was found to occur in abundance in neurons of select brain regions such as the amygdala and hippocampus and was localized principally to LAMP2-positive vesicles (Fig. 4), the staining for which was also increased in these areas (Fig. 3F). Remarkably, GM2-accumulating neurons also exhibited little or no evidence of activity of the GM2-degradative lysosomal hydrolase, β-hexosaminidase (Fig. 3B and D). While this finding provides a straightforward explanation for the increase in GM2 ganglioside, understanding why an NHE6 deficiency leads to such an effect, and why it exhibits such striking neuron type-specificity, are unknown and will require further investigation.

In human brain, GM2 and GM3 gangliosides are normally very minor components and constitute no more than 1–2% of the total amount of gangliosides. Their proportion is even smaller in normal mouse brain. Sequestration of GM2 ganglioside is observed in many lysosomal diseases, most notably in GM2 gangliosidosis, and also in diseases without known defects in glycosphingolipid catabolism, such as Niemann–Pick disease type C and many of the mucopolysaccharidoses (McGlynn *et al.*, 2004; Walkley, 2009; Walkley and Vanier, 2009). This finding has led to the view that this ganglioside, along with GM3 ganglioside, represents sensitive markers of endosomal–lysosomal dysfunction (Walkley, 2004*b*). In the current study, biochemical analysis did not reveal increases in either total GM2 or GM3 gangliosides, but immune labelling clearly showed selective accumulation of GM2 ganglioside in neurons. Given the highly localized nature of this accumulation, it is not

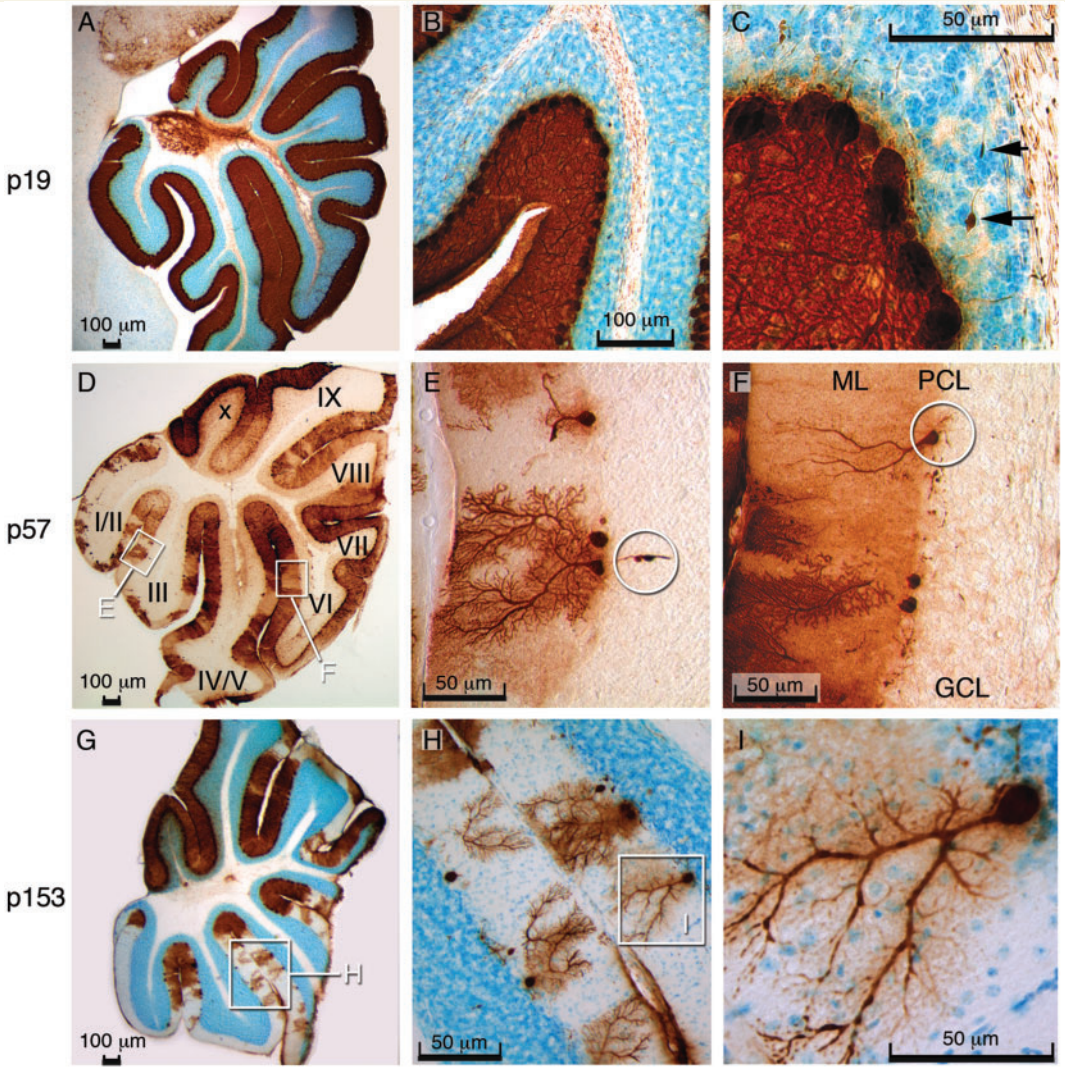

Figure 6 Extensive and progressive loss of Purkinje cells in the mouse cerebellum. (**A–C**) Immunoperoxidase staining for calbindin (brown) with Nissl counterstain (blue) revealed normal cerebellar Purkinje cells in a 19-day-old (p19) *Slc9a6*$^{-/Y}$ animal. The arrows in **C** indicate axonal spheroids. (**D**) Purkinje cell degeneration, particularly noticeable in lobules I/II and III at p57. (**E**) Purkinje cell loss and axonal spheroids (encircled) at p57. (**F**) Purkinje cell that has lost all dendritic branches (ML = molecular layer; PCL = Purkinje cell layer; GCL = granular cell layer). (**G**) Purkinje cell degeneration is extensive with relative sparing of lobules IX and X at p153. (**H**) Purkinje cells in the process of losing dendritic branches. (**I**) Magnified view of insert in **G**.

surprising that biochemical analysis of the entire cerebrum failed to reveal significant differences. In terms of cholesterol, total brain levels are not typically increased in various lysosomal diseases, but conspicuous sequestration of unesterified cholesterol does often occur in individual brain cells, for example in GM2 gangliosidosis and in Niemann–Pick disease type C (Walkley and Vanier, 2009). Cholesterol sequestration is thus another likely indicator of a processing defect in the endosomal–lysosomal system (Walkley and Vanier, 2009). The *Slc9a6* mutant mice were no exception in that unesterified cholesterol often was found in the same neurons storing GM2 ganglioside. However, just as observed in lysosomal diseases (McGlynn *et al.*, 2004; Zhou *et al.*, 2011) the accumulating cholesterol and GM2 ganglioside, while both found in LAMP2-positive vesicles, were not typically co-localized. This finding is believed to be indicative of the heterogeneity of processing within the endosomal–lysosomal system (Zhou *et al.*, 2011). These findings provide further support for the view that *Slc9a6* defects cause disturbances in endosomal–lysosomal processing, which in turn leads to the accumulation of substrates in late endosomes and lysosomes in a manner typical of many lysosomal disorders. Furthermore, while many lysosomal diseases exhibit widespread neuronal involvement, others exhibit storage restricted to select neuronal populations (Walkley, 1998, 2004*a*, *b*) in a manner not dissimilar to findings here in *Slc9a6* deficiency. It is likely that endosomal compromise in NHE6-depleted mice is caused by increased intravesicular acidity. However, in HeLa cells, depletion

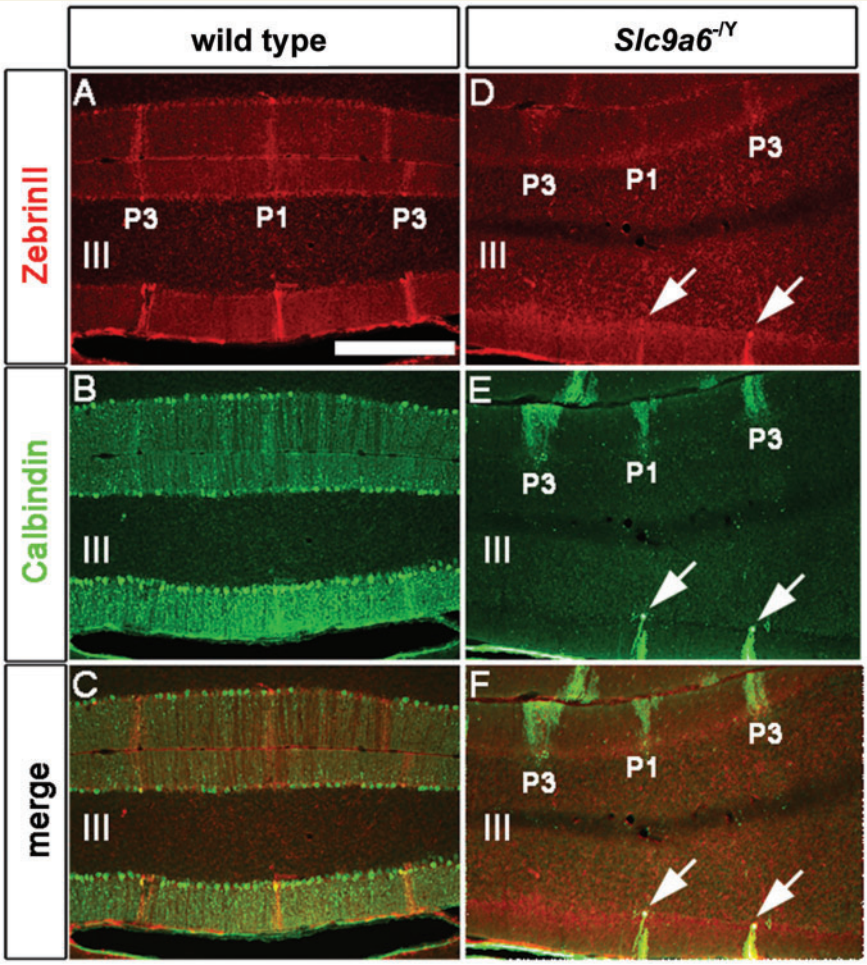

Figure 7 Purkinje cell degeneration was patterned in the cerebellum of *Slc9a6*$^{-/Y}$ mice. (**A**) Zebrin II is expressed in parasagittal stripes of Purkinje cells. (**B**) Calbindin is expressed in all Purkinje cells. (**C**) Merged image of **A** and **B**. (**D**) Zebrin II expression is normal in *Slc9a6*$^{-/Y}$ mice. (**E**) Calbindin expression reveals patterned Purkinje cell degeneration in *Slc9a6*$^{-/Y}$ mice. (**F**) Merged image of **D** and **E** illustrating that all surviving Purkinje cells in *Slc9a6*$^{-/Y}$mice are Zebrin II immunoreactive (see P1 and P3 stripes and white arrows). Lobules are indicated by Roman numerals according to the previous nomenclature. Scale bar: **A** = 500 μm.

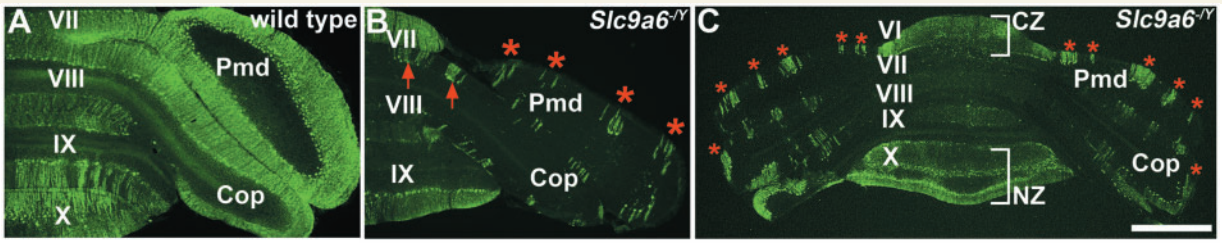

Figure 8 Purkinje cell degeneration was patterned in the cerebellar vermis and hemispheres of *Slc9a6*$^{-/Y}$mice. (**A**) Calbindin is expressed in all Purkinje cells in wild-type mice. (**B**) Calbindin expression reveals parasagittal stripes in the vermis (red arrows) and hemispheres (red asterisks) of *Slc9a6*$^{-/Y}$mice. (**C**) Low power image of an *Slc9a6*$^{-/Y}$animal illustrating: (i) the parasagittal pattern of surviving Purkinje cells in the hemispheres (each stripe is labelled with a red asterisk); and (ii) Purkinje cells in the central zone (CZ, lobules VI/VII) and nodular zone (NZ, lobules IX/X) are resistant to degeneration (white brackets). Scale bar: **C** = 1 mm (=500 μm for **A** and **B**). Cop = copula pyramidis; Pmd = paramedian lobule.

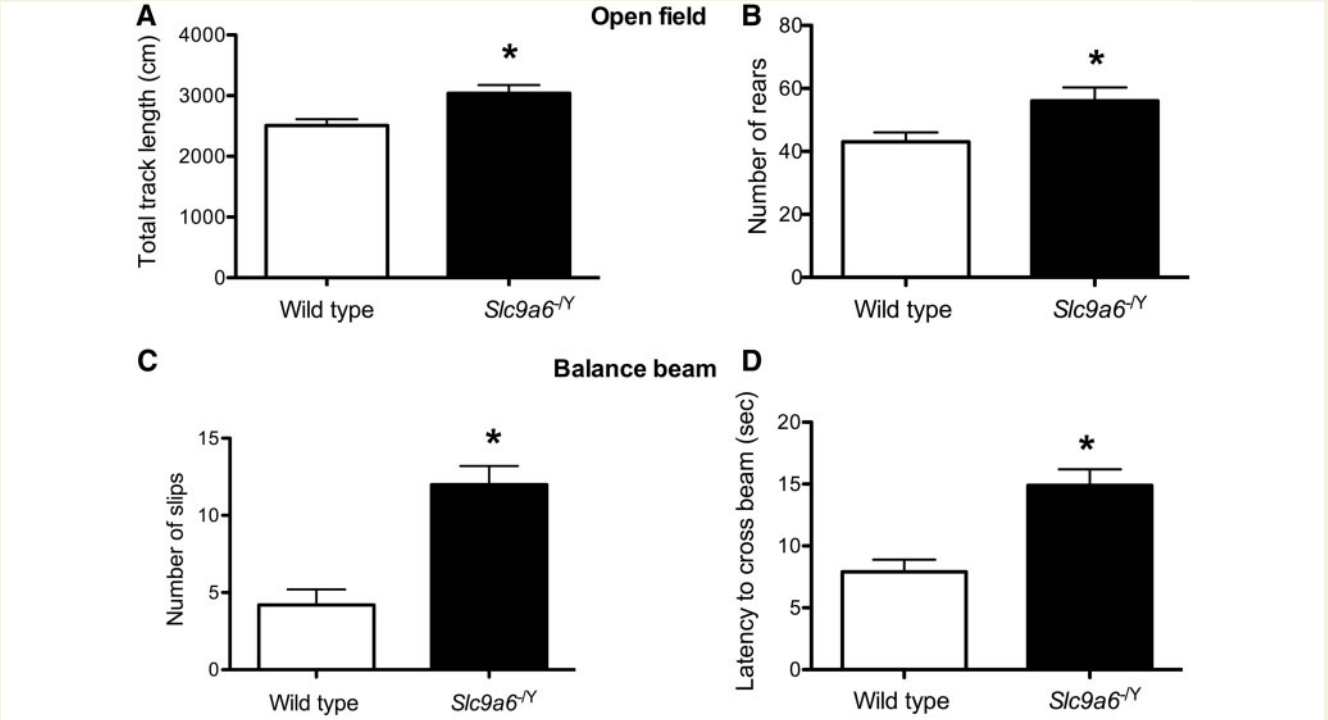

Figure 9 Behavioural studies. Hyperactivity in the open field in *Slc9a6*$^{-/Y}$ mice was demonstrated by (**A**) the significantly higher track length ($P = 0.008$) and (**B**) a significantly increased number of rears ($P = 0.03$). Motor coordination deficits in the *Slc9a6*$^{-/Y}$mice were evident in the balance beam as (**C**) significantly higher number of slips ($P < 0.001$) and (**D**) a longer latency to cross the beam ($P < 0.001$). Asterisk denotes statistically significant difference.

of NHE6 alone did not have any detectable effect on endosomal pH, whereas co-depletion of NHE6 and NHE9 caused enhanced acidification in early endosomes (Roxrud *et al.*, 2009).

Electron microscopy data (Fig. 5) show evidence of accumulating materials within vesicles, as well as possible alterations in a variety of cytoplasmic constituents and further support our contention that *Slc9a6* knockout causes disruption of the endosomal–lysosomal system. Overall, neurons were found to contain occasional dense, membrane-bound aggregates of material or larger non-membrane-bound structures resembling aggresomes (Johnston *et al.*, 1998) or stigmoid bodies (Fujinaga *et al.*, 2009). The membrane-bound GM2 ganglioside-containing lysosomal storage body-like vesicles (Fig. 5H, inset) that were conspicuous in neurons of the amygdala resembled somewhat the concentric multi-lamellar bodies found in some primary ganglioside storage diseases, but not the zebra body characteristic of GM2 ganglioside storage, as for example observed by Stromme *et al.* (1997) or in the mucopolysaccharidoses (McGlynn *et al.*, 2004). Neurons also exhibited unusual alterations in perikaryal distribution of organelles, with some areas near the Golgi and trans-Golgi network showing corralled groups of vesicles and other structures (Fig. 5). Some neuronal nuclei were also heavily lobulated or contained unusually conspicuous nucleoli. Additional electron microscopy studies are warranted to determine the full extent of the impact of NHE6 deficiency on neurons.

Deterioration of organ system functioning is common in lysosomal storage diseases. Although deterioration in clinical status was not observed in our *Slc9a6*$^{-/Y}$ mice, the extensive loss of Purkinje cells in these mice correlates with cerebellar atrophy observed in human *SLC9A6* mutation (Gilfillan *et al.*, 2008; Schroer *et al.*, 2010). Autopsies of several patients with *SLC9A6* mutations have demonstrated marked neuronal loss and gliosis of the globus pallidus, putamen, substantia nigra and cerebellar cortex associated with tau-containing filaments on ultrastructural examination (Garbern *et al.*, 2010). The latter finding was believed to be evidence of abnormal vesicular targeting secondary to NHE6 loss. Based on these studies, we also analysed the *Slc9a6* mutant mice for accumulation of phosphorylated tau, and found small increases in the soluble brain fractions of mutant mice (Supplementary Fig. 2). Interestingly, in Niemann–Pick disease type C, storage of cholesterol and glycosphingolipids in the human disease is consistently accompanied by the presence of hyperphosphorylated tau and neurofibrillary tangles. The mouse model of Niemann–Pick disease type C, however, exhibits only minor tau hyperphosphorylation and no evidence of a frank tauopathy (Walkley and Suzuki, 2004). It is thus conceivable that the tau depositions identified in human brains with *SLC9A6* mutations (Garbern *et al.*, 2010) are a downstream consequence of endosomal–lysosomal dysfunction just as they appear to be in human Niemann–Pick disease type C. Interestingly, some forms of Alzheimer's disease have also recently been reported to exhibit compromise in endosomal–lysosomal function with such abnormalities likely being primary contributors to the brain pathology (Lee *et al.*, 2010).

Involvement of the amygdala

While some lysosomal diseases show more storage of GM2 ganglioside in certain groups of neurons, the singularly abundant level of sequestration observed in amygdala in *Slc9a6*-targeted mice is highly unusual. The amygdala complex is a collection of associated nuclei along an anterior–posterior axis in the human temporal lobe. The basolateral nuclei of the amygdala connect primarily with thalamus and regions of the neocortex and send efferent fibres to the hippocampus (Manns and Eichenbaum, 2008). These nuclei are the main route by which sensory information enters the amygdala and its circuitry is just beginning to be elucidated (Spampanato *et al.*, 2011). In our study, we observed that GM2 ganglioside accumulation was greatest by far in the medial parts of the basolateral nuclei, but why such select neuronal involvement occurred is unknown. Interestingly, GM2 ganglioside accumulation was also noted in hippocampal CA3 and CA4 and dentate gyrus neurons, and neurons of the piriform (entorhinal) cerebral cortex and the fasciola cinereum, all of which represent primitive archicortical and paleocortical brain regions.

In humans, lesions in the amygdala may cause impairment of memory, emotions and learning and its dysfunction is also associated with autism (Mosconi *et al*., 2009). The autistic-like behaviour caused by *SLC9A6* mutation is comparable with that of Rett and Angelman syndromes. Thus, *MECP2*, *UBE3A* and *SLC9A6* are all regarded as autism-related genes (Sutcliffe, 2008). In mice, *Mecp2* plays a key role as a transcriptional repressor in the basolaterol nuclei of the amygdala, mediating the behavioural features of Rett syndrome (Adachi *et al.*, 2009). Interestingly, a mutation in *SLC9A9* was shown to cause autism and seizures in humans (Morrow *et al.*, 2008; Sutcliffe, 2008). *SLC9A9* is also a susceptibility gene for hyperactivity attention deficit disorders (de Silva *et al.*, 2003; Lasky-Su *et al.*, 2008; Markunas *et al.*, 2010). Data on *Slc9a9* knockouts are unavailable, so we do not know if loss of NHE9 also leads to endosomal–lysosomal disruption in the amygdala.

The amygdala and the cerebellum are involved in the neural control of laughter (Parvizi *et al.*, 2007), two anatomical areas that conspicuously are targeted by NHE6 loss of function. Few metabolic diseases are known to show strong predilection for the amygdala. However, an exception is Urbach–Wiethe disease (OMIM #247100), a putative lysosomal disease that particularly may involve the amygdala and is associated with neuropsychiatric symptoms (Goncalves *et al.*, 2010).

Cerebellar degeneration

We have found a number of pathological defects in the cerebellum of *Slc9a6*-targeted mice. Purkinje cell axons exhibited axonal spheroids (Fig. 6C and E) that are swellings on the axon, typically seen in Niemann–Pick disease type C and many other lysosomal diseases (Walkley *et al.*, 2010). The loss of Purkinje cells occurred in parasagittal stripes (Fig. 7). This is not the first demonstration of patterned cell loss in the cerebellum. For example, in the spontaneous mutants 'Nervous', 'Purkinje cell degeneration' and 'Tambaleante', the patterns of surviving Purkinje cells were arranged according to different and reproducible arrays of sagittal bands that were symmetric about the midline (Wassef *et al.*, 1987). In addition, a parasagittal pattern of cell loss/survival was also described in Niemann–Pick disease type C 1 mutant mice (Sarna *et al.*, 2003), and similar loss of Purkinje cells has been observed in other lysosomal diseases (Walkley *et al.*, 2010). The pattern of cell death in our *Slc9a6* mutants corresponded to Niemann–Pick disease type C1 mice and was complementary to the pattern reported in *Nervous* cerebella (Wassef *et al.*, 1987). Therefore, depending on the mutation, the surviving cells are either Zebrin II-immunopositive or Zebrin II-immunonegative. These data suggest that although Purkinje cells are differentially sensitive to genetic defects, different mutations can lead to a fundamental pattern of cell death with topographical features that respect the normal pattern of cerebellar gene expression.

Angelman syndrome—pathways to intellectual disability

Most cases of Angelman syndrome are due to defects in *UBE3A* encoding E6-AP, an E3 ubiquitin ligase that functions in the ubiquitin–proteasome system (Scheffner *et al.*, 1993), a key cellular mechanism for cytosolic protein degradation. Similarities in the profound intellectual disability and related Angelman syndrome features linked to both *UBE3A* and *SLC9A6* mutations could be explained if each protein coded for was integrated within the same intracellular machinery for protein degradation, or if they shared parallel functions in a key mechanism underlying learning and memory. Indeed, this may be the case in terms of the excitatory glutamatergic receptors at dendritic spine synapses. AMPA (α-amino-3-hydroxy-5-methylisoazole-4-proprionic acid) receptors regulate the majority of fast excitatory neurotransmission and are known to undergo rapid constitutive internalization as a consequence of synaptic activity. This turnover or 'cycling' of AMPA receptors is known to play a critical role in synaptic plasticity (Isaac *et al.*, 2007). Recent studies have indicated that proteasomes are present in dendritic spines, where they are believed to function in synaptic development and plasticity (Patrick, 2006). It is also well documented that ubiquitination and proteasomal function play a critical role in endocytosis and signalling (Mukhopadhyay and Riezman, 2007) including removal of surface AMPA receptors (Turrigiano, 2002). However, another mechanism governing synaptic plasticity is through neurotransmitter receptor insertion and removal, followed by reinsertion or degradation, as carried out by endosomes (Carroll *et al.*, 2001). Once internalized, AMPA receptors are sorted from early endosomes to either specialized recycling endosome for re-insertion in the plasmalemma or, are trafficked to the endosomal–lysosomal system for degradation. Thus, it will be important to determine whether defects in E6-AP and NHE6 converge at the dendritic spine and similarly compromise the recycling of AMPA receptors. Interestingly, pyramidal and multipolar spiny neurons in cerebral cortex, amygdala and other brain regions in lysosomal diseases with endosomal–lysosomal GM2 ganglioside sequestration similar to that reported here are also known to be characterized by abnormal (ectopic) dendritogenesis, with the clinical syndromes in these disorders also characterized by intellectual disability (Walkley, 1998, 2004*b*).

Conclusion

The *Slc9a6* knockout mouse used in this study appears to be a useful model to reveal some of the pathogenic processes leading to the human phenotypes caused by *SLC9A6* mutation and to the possible pathogenic cascade features underlying Angelman syndrome. Foremost, we documented that NHE6 deficiency leads to an unexpected reduction in β-hexosaminidase and to the accumulation of GM2 ganglioside and cholesterol in select neuronal populations, particularly those of the amygdala and hippocampus, and to the formation of axonal spheroids and Purkinje cell degeneration in the cerebellum. Both these cellular pathological features are reminiscent of those observed in primary lysosomal disorders and suggest that the *SLC9A6* mutations may be causing a heretofore unrecognized lysosomal storage disease.

Acknowledgements

We are grateful to Marie T. Vanier, National Institute of Health and Medical Research (INSERM) and Hopitâux de Lyon, France, for biochemical analysis of brain gangliosides. Sharon Zhou, Bin Cui, Ryan Lippell and Samrawit A. Gebre, Albert Einstein College of Medicine, New York, USA, are thanked for technical assistance.

Funding

Support from VIRUUS, the Research Council at Oslo University Hospital (to P.S.); New Investigator Start-Up funds (to R.V.S.); National Institute of Health grant (HD045561 to S.U.W).

Supplementary material

Supplementary material is available at *Brain* online.

References

Adachi M, Autry AE, Covington HE III, Monteggia LM. MeCP2-mediated transcription repression in the basolateral amygdala may underlie heightened anxiety in a mouse model of Rett syndrome. J Neurosci 2009; 29: 4218–27.

Ahn AH, Dziennis S, Hawkes R, Herrup K. The cloning of zebrin II reveals its identity with aldolase C. Development 1994; 120: 2081–90.

Ali A, Feroze AH, Rizvi ZH, Rehman TU. Consanguineous marriage resulting in homozygous occurrence of X-linked retinoschisis in girls. Am J Ophthalmol 2003; 136: 767–9.

Bergeron MJ, Simonin A, Burzle M, Hediger MA. Inherited epithelial transporter disorders-an overview. J Inherit Metab Dis 2008; 31: 178–87.

Brett CL, Tukaye DN, Mukherjee S, Rao R. The yeast endosomal Na+K+/H+ exchanger Nhx1 regulates cellular pH to control vesicle trafficking. Mol Biol Cell 2005; 16: 1396–405.

Brett CL, Wei Y, Donowitz M, Rao R. Human Na(+)/H(+) exchanger isoform 6 is found in recycling endosomes of cells, not in mitochondria. Am J Physiol Cell Physiol 2002; 282: C1031–41.

Brochu G, Maler L, Hawkes R. Zebrin II: a polypeptide antigen expressed selectively by Purkinje cells reveals compartments in rat and fish cerebellum. J Comp Neurol 1990; 291: 538–52.

Carroll RC, Beattie EC, von Zastrow M, Malenka RC. Role of AMPA receptor endocytosis in synaptic plasticity. Nat Rev Neurosci 2001; 2: 315–24.

Casey JR, Grinstein S, Orlowski J. Sensors and regulators of intracellular pH. Nat Rev Mol Cell Biol 2010; 11: 50–61.

Choleris E, Thomas AW, Kavaliers M, Prato FS. A detailed ethological analysis of the mouse open field test: effects of diazepam, chlordiazepoxide and an extremely low frequency pulsed magnetic field. Neurosci Biobehav Rev 2001; 25: 235–60.

Christianson AL, Stevenson RE, van der Meyden CH, Pelser J, Theron FW, van Rensburg PL, et al. X linked severe mental retardation, craniofacial dysmorphology, epilepsy, ophthalmoplegia, and cerebellar atrophy in a large South African kindred is localised to Xq24-q27. J Med Genet 1999; 36: 759–66.

Dahlin A, Royall J, Hohmann JG, Wang J. Expression profiling of the solute carrier gene family in the mouse brain. J Pharmacol Exp Ther 2009; 329: 558–70.

Davidson CD, Ali NF, Micsenyi MC, Stephney G, Renault S, Dobrenis K, et al. Chronic cyclodextrin treatment of murine Niemann-Pick C disease ameliorates neuronal cholesterol and glycosphingolipid storage and disease progression. PLoS One 2009; 4: e6951.

de Silva MG, Elliott K, Dahl HH, Fitzpatrick E, Wilcox S, Delatycki M, et al. Disruption of a novel member of a sodium/hydrogen exchanger family and DOCK3 is associated with an attention deficit hyperactivity disorder-like phenotype. J Med Genet 2003; 40: 733–40.

Ennaceur A, Meliani K. A new one-trial test for neurobiological studies of memory in rats. III. Spatial vs. non-spatial working memory. Behav Brain Res 1992; 51: 83–92.

Fujinaga R, Takeshita Y, Uozumi K, Yanai A, Yoshioka K, Kokubu K, et al. Microtubule-dependent formation of the stigmoid body as a cytoplasmic inclusion distinct from pathological aggresomes. Histochem Cell Biol 2009; 132: 305–18.

Garbern JY, Neumann M, Trojanowski JQ, Lee VM, Feldman G, Norris JW, et al. A mutation affecting the sodium/proton exchanger, SLC9A6, causes mental retardation with tau deposition. Brain 2010; 133: 1391–402.

Gilfillan GD, Selmer KK, Roxrud I, Smith R, Kyllerman M, Eiklid K, et al. SLC9A6 mutations cause X-linked mental retardation, microcephaly, epilepsy, and ataxia, a phenotype mimicking Angelman syndrome. Am J Hum Genet 2008; 82: 1003–10.

Goncalves FG, de Melo MB, de LMV, Barra FR, Figueroa RE. Amygdalae and striatum calcification in lipoid proteinosis. Am J Neuroradiol 2010; 31: 88–90.

Goodman LA, Walkley SU. Elevated GM2 ganglioside is associated with dendritic proliferation in normal developing neocortex. Brain Res Dev Brain Res 1996; 93: 162–71.

He L, Vasiliou K, Nebert DW. Analysis and update of the human solute carrier (SLC) gene superfamily. Hum Genomics 2009; 3: 195–206.

Isaac JT, Ashby M, McBain CJ. The role of the GluR2 subunit in AMPA receptor function and synaptic plasticity. Neuron 2007; 54: 859–71.

Johnston JA, Ward CL, Kopito RR. Aggresomes: a cellular response to misfolded proteins. J Cell Biol 1998; 143: 1883–98.

Larsell O. The morphogenesis and adult pattern of the lobules and fissures of the cerebellum of the white rat. J Comp Neurol 1952; 97: 281–356.

Lasky-Su J, Neale BM, Franke B, Anney RJ, Zhou K, Maller JB, et al. Genome-wide association scan of quantitative traits for attention deficit hyperactivity disorder identifies novel associations and confirms candidate gene associations. Am J Med Genet B Neuropsychiatr Genet 2008; 147B: 1345–54.

Lee JH, Yu WH, Kumar A, Lee S, Mohan PS, Peterhoff CM, et al. Lysosomal proteolysis and autophagy require presenilin 1 and are disrupted by Alzheimer-related PS1 mutations. Cell 2010; 141: 1146–58.

Lein ES, Hawrylycz MJ, Ao N, Ayres M, Bensinger A, Bernard A, et al. Genome-wide atlas of gene expression in the adult mouse brain. Nature 2007; 445: 168–76.

Manns RJ, Eichenbaum H. Learning and memory. In: Squire LR, Berg D, Bloom FE, du Lac S, Gosh A, Spitzer NC, editors. Fundamental neuroscience. Amsterdam: Elsevier; 2008. p. 1153–77.

Markunas CA, Quinn KS, Collins AL, Garrett ME, Lachiewicz AM, Sommer JL, et al. Genetic variants in SLC9A9 are associated with measures of attention-deficit/hyperactivity disorder symptoms in families. Psychiatr Genet 2010; 20: 73–81.

McGlynn R, Dobrenis K, Walkley SU. Differential subcellular localization of cholesterol, gangliosides, and glycosaminoglycans in murine models of mucopolysaccharide storage disorders. J Comp Neurol 2004; 480: 415–26.

Micsenyi MC, Dobrenis K, Stephney G, Pickel J, Vanier MT, Slaugenhaupt SA, et al. Neuropathology of the Mcoln1(-/-) knockout mouse model of mucolipidosis type IV. J Neuropathol Exp Neurol 2009; 68: 125–35.

Morrow EM, Yoo SY, Flavell SW, Kim TK, Lin Y, Hill RS, et al. Identifying autism loci and genes by tracing recent shared ancestry. Science 2008; 321: 218–23.

Mosconi MW, Cody-Hazlett H, Poe MD, Gerig G, Gimpel-Smith R, Piven J. Longitudinal study of amygdala volume and joint attention in 2- to 4-year-old children with autism. Arch Gen Psychiatry 2009; 66: 509–16.

Mukhopadhyay D, Riezman H. Proteasome-independent functions of ubiquitin in endocytosis and signaling. Science 2007; 315: 201–5.

Nakamura N, Tanaka S, Teko Y, Mitsui K, Kanazawa H. Four Na+/H+ exchanger isoforms are distributed to Golgi and post-Golgi compartments and are involved in organelle pH regulation. J Biol Chem 2005; 280: 1561–72.

Nass R, Cunningham KW, Rao R. Intracellular sequestration of sodium by a novel Na+/H+ exchanger in yeast is enhanced by mutations in the plasma membrane H+-ATPase. Insights into mechanisms of sodium tolerance. J Biol Chem 1997; 272: 26145–52.

Ohgaki R, van ISC, Matsushita M, Hoekstra D, Kanazawa H. Organellar Na+/H+ exchangers: novel players in organelle pH regulation and their emerging functions. Biochemistry 2011; 50: 443–50.

Ozol K, Hayden JM, Oberdick J, Hawkes R. Transverse zones in the vermis of the mouse cerebellum. J Comp Neurol 1999; 412: 95–111.

Parvizi J, Joseph J, Press DZ, Schmahmann JD. Pathological laughter and crying in patients with multiple system atrophy-cerebellar type. Mov Disord 2007; 22: 798–803.

Patrick GN. Synapse formation and plasticity: recent insights from the perspective of the ubiquitin proteasome system. Curr Opin Neurobiol 2006; 16: 90–4.

Paxinos G, Watson S. The rat brain in stereotactic coordinates. 2nd edn. San Diego: Academic Press; 1986.

Roxrud I, Raiborg C, Gilfillan GD, Stromme P, Stenmark H. Dual degradation mechanisms ensure disposal of NHE6 mutant protein associated with neurological disease. Exp Cell Res 2009; 315: 3014–27.

Sarna JR, Larouche M, Marzban H, Sillitoe RV, Rancourt DE, Hawkes R. Patterned Purkinje cell degeneration in mouse models of Niemann-Pick type C disease. J Comp Neurol 2003; 456: 279–91.

Scheffner M, Huibregtse JM, Vierstra RD, Howley PM. The HPV-16 E6 and E6-AP complex functions as a ubiquitin-protein ligase in the ubiquitination of p53. Cell 1993; 75: 495–505.

Schroer RJ, Holden KR, Tarpey PS, Matheus MG, Griesemer DA, Friez MJ, et al. Natural history of Christianson syndrome. Am J Med Genet Part B 2010; 152A: 2775–83.

Sillitoe RV, Hawkes R. Whole-mount immunohistochemistry: a high-throughput screen for patterning defects in the mouse cerebellum. J Histochem Cytochem 2002; 50: 235–44.

Sillitoe RV, Joyner AL. Morphology, molecular codes, and circuitry produce the three-dimensional complexity of the cerebellum. Annu Rev Cell Dev Biol 2007; 23: 549–77.

Sillitoe RV, Stephen D, Lao Z, Joyner AL. Engrailed homeobox genes determine the organization of Purkinje cell sagittal stripe gene expression in the adult cerebellum. J Neurosci 2008; 28: 12150–62.

Spampanato J, Polepalli J, Sah P. Interneurons in the basolateral amygdala. Neuropharmacology 2011; 60: 765–73.

Stanley JL, Lincoln RJ, Brown TA, McDonald LM, Dawson GR, Reynolds DS. The mouse beam walking assay offers improved sensitivity over the mouse rotarod in determining motor coordination deficits induced by benzodiazepines. J Psychopharmacol 2005; 19: 221–7.

Stromme P, Mansson JE, Scott H, Skullerud K, Hovig T. Encephaloneuropathy with lysosomal zebra bodies and GM2 ganglioside storage. Pediatr Neurol 1997; 16: 141–4.

Sutcliffe JS. Genetics. Insights into the pathogenesis of autism. Science 2008; 321: 208–9.

Turrigiano GG. A recipe for ridding synapses of the ubiquitous AMPA receptor. Trends Neurosci 2002; 25: 597–8.

Walkley SU. Cellular pathology of lysosomal storage disorders. Brain Pathology 1998; 8: 175–93.

Walkley SU. Pathogenic cascades and brain function. In: Platt FM, Walkley SU, editors. Lysosomal disorders of the brain. Oxford: Oxford University Press; 2004a.

Walkley SU. Secondary accumulation of gangliosides in lysosomal storage disorders. Semin Cell Dev Biol 2004b; 15: 433–44.

Walkley SU. Pathogenic cascades in lysosomal disease-Why so complex? J Inherit Metab Dis 2009; 32: 181–9.

Walkley SU, Sikora J, Micsenyi M, Davidson C, Dobrenis K. Lysosomal compromise and brain dysfunction: examining the role of neuroaxonal dystrophy. Biochem Soc Trans 2010; 38: 1436–41.

Walkley SU, Suzuki K. Consequences of NPC1 and NPC2 loss of function in mammalian neurons. Biochim Biophys Acta 2004; 1685: 48–62.

Walkley SU, Vanier MT. Secondary lipid accumulation in lysosomal disease. Biochim Biophys Acta 2009; 1793: 726–36.

Wassef M, Sotelo C, Cholley B, Brehier A, Thomasset M. Cerebellar mutations affecting the postnatal survival of Purkinje cells in the mouse disclose a longitudinal pattern of differentially sensitive cells. Dev Biol 1987; 124: 379–89.

Williams CA, Beaudet AL, Clayton-Smith J, Knoll JH, Kyllerman M, Laan LA, et al. Angelman syndrome 2005: updated consensus for diagnostic criteria. Am J Med Genet 2006; 140: 413–8.

Zhou S, Davidson C, McGlynn R, Stephney G, Dobrenis K, Vanier MT, et al. Endosomal/lysosomal processing of gangliosides affect neuronal sequestration in Niemann-Pick disease type C. Am J Pathol 2011; 179: 890–902.